De Novo Variants in *LMNB1* Cause Pronounced Syndromic Microcephaly and Disruption of Nuclear Envelope Integrity

Francesca Cristofoli,[1,12] Tonya Moss,[2,12] Hannah W. Moore,[3] Koen Devriendt,[1] Heather Flanagan-Steet,[2] Melanie May,[2] Julie Jones,[2] Filip Roelens,[4] Carmen Fons,[5] Anna Fernandez,[5] Loreto Martorell,[6] Angelo Selicorni,[7] Silvia Maitz,[8] Giuseppina Vitiello,[9] Gerd Van der Hoeven,[10] Steven A. Skinner,[3] Mathieu Bollen,[10] Joris R. Vermeesch,[1] Richard Steet,[2,*] and Hilde Van Esch[1,11,*]

Summary

Lamin B1 plays an important role in the nuclear envelope stability, the regulation of gene expression, and neural development. Duplication of *LMNB1*, or missense mutations increasing *LMNB1* expression, are associated with autosomal-dominant leukodystrophy. On the basis of its role in neurogenesis, it has been postulated that *LMNB1* variants could cause microcephaly. Here, we confirm this hypothesis with the identification of *de novo* mutations in *LMNB1* in seven individuals with pronounced primary microcephaly (ranging from −3.6 to −12 SD) associated with relative short stature and variable degree of intellectual disability and neurological features as the core symptoms. Simplified gyral pattern of the cortex and abnormal corpus callosum were noted on MRI of three individuals, and these individuals also presented with a more severe phenotype. Functional analysis of the three missense mutations showed impaired formation of the LMNB1 nuclear lamina. The two variants located within the head group of LMNB1 result in a decrease in the nuclear localization of the protein and an increase in misshapen nuclei. We further demonstrate that another mutation, located in the coil region, leads to increased frequency of condensed nuclei and lower steady-state levels of lamin B1 in proband lymphoblasts. Our findings collectively indicate that *de novo* mutations in *LMNB1* result in a dominant and damaging effect on nuclear envelope formation that correlates with microcephaly in humans. This adds *LMNB1* to the growing list of genes implicated in severe autosomal-dominant microcephaly and broadens the phenotypic spectrum of the laminopathies.

The nuclear lamina (NL) is a filamentous network of proteins lying beneath the inner nuclear membrane of most metazoan cells.[1] Although originally thought to be an inert structural scaffold for the nuclear envelope, several studies have demonstrated complex roles for the NL in cell metabolism. Besides contributing to the mechanical stability of the nuclear envelope, controlling the position of nuclear pore complexes, and anchoring and organizing the chromatin, the NL is involved in the regulation of DNA replication, transcription, and repair in cell cycle progression, nuclear migration, and apoptosis.[2–6] The major components of the NL are type V intermediate filament proteins grouped in two distinct classes, namely A- and B-type lamins. In mammals, A-type lamins (A, AΔ10, C, and C2) are generated by alternative splicing of a single locus (*LMNA* in humans [MIM: 150330]) and expressed primarily in a subset of differentiated cells but also at low abundance early in development. Conversely, B-type lamins are encoded by two distinct genes (*LMNB1* [MIM: 150340] and *LMNB2* [MIM: 150341] in humans) and expressed in almost all known cell types beginning at earliest stages of development.[3,7,8] Lamin-deficient mouse models have been used to elucidate their roles during development.[9–11] B-type lamin-deficient mice are neonatal lethal and display characteristic brain abnormalities that point to an essential role for B-type lamins in proper organogenesis as well as in neuronal migration and patterning during brain development. Both LMNB1- and LMNB2-deficient mice—either conventional or forebrain-specific—display neuronal migration and cortical layering defects. In both animal models, the cellularity of the forebrain is markedly reduced, suggesting compromised survival of neurons. These defects are probably due to a weakened NL that interferes with proper nucleokinesis, the nuclear translocation process required for neuronal migration during corticogenesis, resulting in turn in nuclear membrane ruptures that result in interspersion of nuclear and cytoplasmic contents and ultimately cell death.[11] Lamin B-deficient neurons are characterized by aberrant

---

[1]Center for Human Genetics, University Hospitals Leuven, Herestraat 49, 3000 Leuven, Belgium; [2]JC Self Research Institute, Greenwood Genetic Center, 113 Gregor Mendel Circle, Greenwood, SC 29646, USA; [3]Greenwood Genetic Center, 106 Gregor Mendel Circle, Greenwood, SC 29646, USA; [4]Pediatric Neurology, Department of Pediatrics, AZ Delta, Brugsesteenweg 90, 8800 Roeselare, Belgium; [5]Pediatric Neurology Department, Sant Joan de Déu Hospital, Passeig de Sant Joan de Déu 2, 08950 Barcelona, Spain; [6]Department of Genetic and Molecular Medicine IPER, Institut de Recerca, Sant Joan de Déu Hospital, Passeig de Sant Joan de Déu 2, 08950 Barcelona, Spain; [7]Pediatric Department, ASST Lariana, Sant'Anna Hospital, Via Ravona 20, 22042 Como, Italy; [8]Clinical Pediatric Genetics Unit, MBBM Foundation, S. Gerardo Hospital, Via Pergolesi 33, 20900 Monza, Italy; [9]Department of Translational Medicine and Molecular Medicine and Medical Biotechnologies, Federico II University, via Pansini 5, 80131 Naples, Italy; [10]Laboratory of Biosignalling & Therapeutics, Department of Cellular and Molecular Medicine, KU Leuven, Herestraat 49, 3000 Leuven, Belgium; [11]Laboratory for the Genetics of Cognition, Department of Human Genetics, KU Leuven, Herestraat 49, 3000 Leuven, Belgium
[12]These authors contributed equally
*Correspondence: hilde.vanesch@uzleuven.be (H.V.E.), rsteet@ggc.org (R.S.)
https://doi.org/10.1016/j.ajhg.2020.08.015.

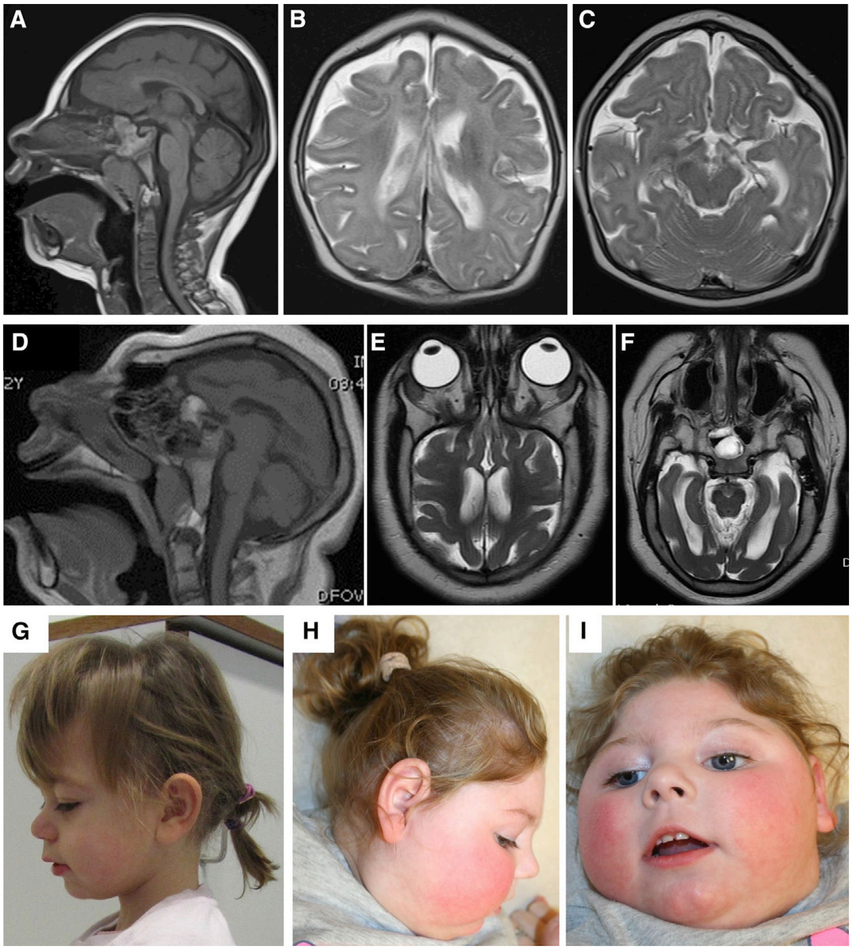

Figure 1. Brain Imaging and Clinical Findings

(A–C) T2-weighted MRI images of affected individual 1 showing a gracile corpus callosum in addition to microcephaly.

(D–F) T2-weighted MRI images of affected individual 6 showing a simplified gyral pattern and dysgenesis of the corpus callosum in addition to extreme microcephaly.

(G) Clinical picture of affected individual 2 at age 3 years showing the microcephaly, small chin, and short nose.

(H and I) Clinical pictures of affected individual 3 showing pronounced microcephaly, long philtrum, short nose, and small chin.

nuclear morphology, abnormal spindle orientation, cell cycle defects, and asymmetric distribution of other nuclear membrane components.[9,12–17] LMNB1 is specifically required for dendritic development in primary mouse cortical neurons,[18] proper differentiation of murine neural stem cells into neurons and astroglial-like cells,[19] and the formation of functional olfactory sensory neurons.[20] On the basis of these *in vitro* and animal data, it has been anticipated that *LMNB1* mutations may contribute to microcephaly in humans.[13–15,21]

In humans, duplication of *LMNB1* causes adult-onset autosomal-dominant leukodystrophy (ADLD [MIM: 169500]).[22] More recently, an individual with a *de novo* c.85C>T (p.Arg29Trp) *LMNB1* variant presenting with cerebellar ataxia and vanishing white matter disease of the cerebellum has been described.[23] Here, we describe seven individuals with novel variants in *LMNB1*, all presenting with pronounced primary microcephaly (ranging from −3.6 to −12 SD) associated with relative short stature and a variable degree of intellectual disability as the core symptoms (Figure 1); these individuals were from five different families. In three individuals, simplified gyral pattern of the cortex and abnormal corpus callosum were noted on MRI (Figure 1). These individuals also showed a more severe neurological phenotype with severe feeding difficulties, spasticity, epilepsy, and neurogenic scoliosis. Individuals 1 and 2 were diagnosed as part of a research project on syndromic microcephaly. Individuals 3–7 were identified and recruited via GeneMatcher.[24] An overview of the clinical features present in the affected individuals is presented in Table 1. More detailed clinical descriptions are provided in the Supplemental Notes.

All studies were approved by the respective ethical committees of the collaborating institutions and performed on genomic DNA extracted from the index and the parents. The parents of subjects provided consent for genetic studies and publication of photographs shown in this study. The various mutations were identified via trio whole-exome sequencing (WES; individuals 1, 3, and 4) or by custom-designed gene panel (individuals 5–7), and technical details are provided in Table S1. In individual 1, a *de novo* missense mutation, c.455C>G, in exon 2 of *LMNB1* (GenBank: NM_005573.3; MIM: 150340) was identified, leading to a p. Ala152Gly change (NP_005564.1). Individuals 3 and 4 each carry a *de novo* mutation, c.97A>G and c.124C>T resulting in p.Lys33Glu and p.Arg42Trp, respectively, in exon 1 of *LMNB1* (Table 1). The location of the mutations is shown in Figure 2A, and all three residues are highly conserved and predicted to be deleterious by various *in silico* methods (Table S2). Individuals 5, 6, and 7 belong to an Arabic sibship, and trio WES identified the same splice mutation, c.939+1G>A, in all three affected children. Further analysis confirmed mosaicism for the c.939+1G>A mutation (15%) in the blood of the father. Human Splicing Finder v.3.1 predicts that this variant disrupts the exon 5 consensus donor splice site, which might result in exon skipping. However, the mutation could also uncover a neighboring exonic or intronic cryptic splice site.[25] *In silico* prediction via the NNSplice[26] and the Alternative Splice Site Predictor[27] software tools indeed revealed a weaker

Table 1. Overview of Clinical Features

	Individual 1	Individual 2	Individual 3	Individual 4	Individual 5	Individual 6	Individual 7
LMNB1 (NM_005573.3) genomic variation GRCh37	exon2: c.455C>G	5q23.2(126,149,952-126,159,137)x1mat	exon1: c.97A>G	exon 1: c.124C>T	c.939+1G>A splice variant		
Protein change	p.Ala152Gly	in-frame p.Ser314_Thr497del	p.Lys33Glu	p.Arg42Trp	elongation of exon 5, introducing 6 novel amino acids?		
Inheritance	*de novo*	maternal	*de novo*	*de novo*	father 15% mosaic for the mutation		
Gender	m	f	f	f	f	m	m
Ethnicity	Caucasian	Caucasian	Caucasian	Caucasian	Arabic	Arabic	Arabic
Birth Parameters							
OFC at birth	25 cm, term	32 cm, term	28 cm, preterm 35 weeks	29 cm, term	N/A	28.5 cm, term	27.5 cm, term
Length at birth	46 cm	51 cm	42 cm	48.9 cm	N/A	N/A	48 cm
Weight at birth	2610 g	3460 g	2190 g	2890 g	N/A	2500 g	2700 g
Growth latest assessment	9 years 6 months	6 years	5 years 7 months	2 years 8 months	1 year 8 months	11 years 11 months	10 years 6 months
Length	122 cm (−2.7 SD)	119.5 cm (+0.7 SD)	92 cm (−4.8 SD)	81 cm (−2.6 SD)	77 cm (−2.4 SD)	122 cm (−4 SD)	125.34 cm (−2.5 SD)
OFC	42 cm (−6.8 SD)	45.1 cm (−3.6 SD)	36.5 cm (−12 SD)	36.1 cm (−12 SD)	35 cm (−4.4 SD)	40 cm (−10 SD)	39 cm (−10 SD)
Facial Features							
Facial dysmorphism	no	pronounced and long philtrum, short nose, trigonocephaly	prominent nasal root, protruding tongue	fullness glabellar region, bitemporal narrowing, prominent eyes and eyelashes, upslanting palpebral fissures	no	gingival hypertrophy	gingival hypertrophy
Neurological							
Degree of DD/ID	moderate to severe	mild	severe	significant developmental delay	significant developmental delay	severe	severe
Brain imaging (MRI)	small brain, normal structures	small brain, normal structures	pachygyria, thin corpus callosum	simplified gyral pattern, dysgenesis of corpus callosum	N/A	simplified gyral pattern, dysgenesis of the corpus callosum	simplified gyral pattern
Neurological abnormalities	no	no	spasticity limbs, inability to walk	seizures (controlled)	seizures (controlled), hypotonia	seizures (controlled), severe axial hypotonia, spastic tetraparesis, no language or communication	seizures (controlled), severe axial hypotonia, spastic tetraparesis, no language or communication
Visual impairment	no	no	no	suspected cortical visual impairment	N/A	cortical visual impairment	cortical visual impairment
Skeletal abnormalities	no	no	scoliosis	no	mild scoliosis	severe scoliosis	severe scoliosis
Gastro-intestinal abnormalities	feeding difficulties	no	feeding difficulties	feeding difficulties, G-tube	no	feeding difficulties, G-tube	feeding difficulties, G-tube
Other	none	OFC mother 50.5 cm (−2.5 SD), low educational level, long philtrum	patent foramen ovale	recurrent pneumonia	none	recurrent pneumonia	recurrent pneumonia

(*Continued on next page*)

Table 1. ***Continued***

	Individual 1	Individual 2	Individual 3	Individual 4	Individual 5	Individual 6	Individual 7
Chromosomal microarray	normal (OGT Cytosure)	intragenic *LMNB1* deletion (OGT Cytosure)	normal (Agilent 180k Hg19)	15q25.3(85,811,682-86,140,453)x3 pat (VOUS; CytoScan DX)	N/A	17p13.3 (954,760-1,235,739)x3 (VOUS; CMA-ISCA)	normal

m, male; f, female; N/A, not assessed; OFC, occipitofrontal circumference; VOUS, variant of unknown significance.

cryptic donor splice sequence 18 nucleotides downstream of the canonical site, which could result in a partial intronic retention and extension of exon 5 by six novel amino acids (Figure 2B). Unfortunately, we were unable to test this hypothesis because the family was unavailable for further RNA studies. None of the above identified variants is present in the dbSNP, 1000 Genomes, Leiden Open Variation Database (LOVD) 3.1, NHLBI Exome Sequencing Project (ESP), or gnomAD databases. Variants have been deposited in ClinVar and have the accession numbers SCV001296959–SCV001296963.

In individual 2, an intragenic heterozygous *LMNB1* deletion was identified by chromosomal microarrays (OGT Cytosure 180k, v3 array). This deletion was inherited from an equally affected mother in whom it occurred *de novo*. The phenotype in individual 2 is milder with a head circumference at −3.6 SD and mild-to-borderline cognitive deficit compared to the other individuals. The deletion spans exons 6–8 of the gene, resulting in a 552-amino-acids in-frame deletion (p.Ser314_Thr497), possibly resulting in a shorter version of the protein noticeably lacking the nuclear localization signal (NLS) (Figure 2). To our knowledge, no other intragenic deletion only affecting *LMNB1* has been reported in any of the large CNV databases (Decipher, Ensembl Genome Browser). On the contrary, several individuals with large contiguous gene deletions on chromosome 5q23.2, including deletion of *LMNB1,* have been reported and only in one affected individual, harboring a 134 Mb deletion, microcephaly was noted (Decipher ID: 282760). This argues against haploinsufficiency as a potential mechanism for the phenotypes in this cohort because *LMNB1* seems to be tolerant to loss of function (pLI score 0.55). Therefore, we predict that a dominant-negative effect of the different *de novo* mutations is more likely.

To investigate the functional significance of the identified *LMNB1* variants, we introduced cDNAs coding for the different missense changes into a *LMNB1*-null HeLa cell line and analyzed the ability of these variant lamin B1 molecules to form an NL. Two variants (p.Lys33Glu and p.Arg42Trp) lie within or proximal to the head domain of the protein, whereas p.Ala152Gly resides within the first coil domain (coil 1B, Figure 2A). Biochemical validation of the *LMNB1*-null HeLa cell line demonstrated complete loss of lamin B1 but no change in the amount of lamin A/C as gauged by immunoblot (Figure 3A). Immunofluorescent staining of both lamin B1 and lamin A/C confirmed the absence of lamin B1 and also showed that the NL formed by lamin A/C and overall nuclear morphology is not obviously altered in the null line (Figure 3B). We performed transfection of *LMNB1* variant cDNAs into *LMNB1*-null HeLa cells followed by immunoblot analysis to look at the amount and mobility of lamin B1 (Figures 3C and 3D). In all cases, the transfection led to a significant increase (∼10- to 15-fold) in overall lamin B1 and there were no differences in the corresponding steady-state level of lamin A/C. Lamin B1 ran as a single band at 65 kDa, slightly higher than the faint lamin B1 detected in the parental HeLa cell line. A consistent reduction in steady-state level of p.Ala152Gly lamin B1 was observed despite the introduction of equivalent cDNA amount, suggesting the possible instability of this lamin B1 variant (Figure 3E).

We then performed immunofluorescence staining on the transfected *LMNB1*-null cells to evaluate whether the missense variants alter the formation of the lamin B1 NL (Figure 4). Quantification revealed a much higher abundance of cells with an abnormal nuclear lamina percentage when any of the three missense variants were expressed compared to the wild type (WT). Both the p.Lys33Glu and p.Arg42Trp lamina also appeared diffuse and poorly formed: there was no discrete boundary and dispersion of lamin B1 throughout the cell. In many cells with an abnormal lamina, aggregates of lamin B1 were observed. The lamin A/C NL was variably affected in these transfected cells. An altered morphology of the lamin B1 lamina was noted in cells transfected with the p.Ala152Gly-encoding cDNA, but there was not the same loss of boundary and diffusion seen with the other two variants. The lamin A/C NL in the p.Ala152Gly-transfected cells was ruffled and irregular, suggestive of a more global disruption of the envelope (Figure 4A). In light of lamin B1's established role in the maintenance of nuclear morphology, we also analyzed the morphology of the nucleus in the transfected cells, observing a significant increase in the number of cells with a bi-/multi-lobed phenotype with both p.Lys33Glu- and p.Arg42Trp-encoding cDNA (Figure 4B). These data support the idea that the NL is disrupted when these variant lamin B1 proteins are present, resulting in a misshapen and irregular nuclear structure. This increase was less pronounced in the HeLa cells transfected with cDNA encoding p.Ala152Gly; these cells instead showed an increase in the percentage of cells with condensed nuclei. These condensed and often smaller nuclei were noted at lower frequency in the other transfected cells and may arise as a result of overexpression.

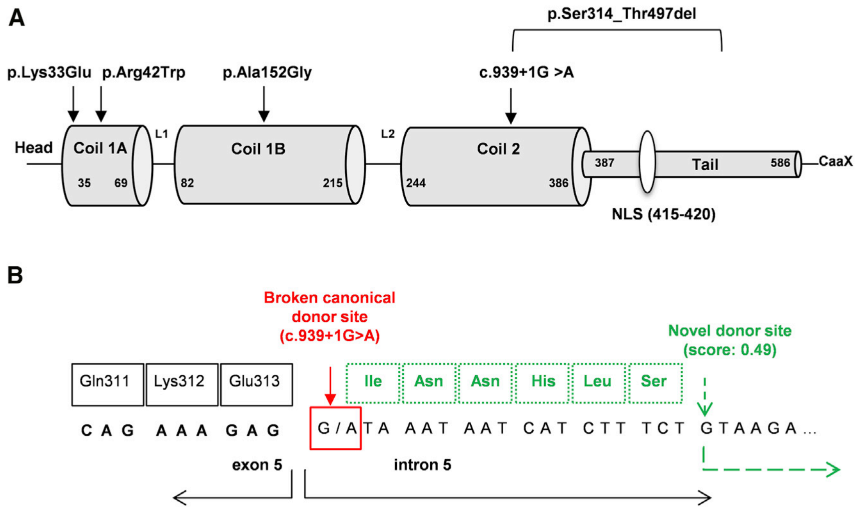

Figure 2. Overview of the Locations of the *LMNB1* Mutations and *In Silico* Prediction of the Effect of the Splice Mutation

(A) Schematic drawing of LMNB1 showing the different coil, head, and tail domains, as well as the localization of the NLS. The different novel mutations and the intragenic deletion are displayed above.

(B) Schematic of the effect of the c.939+1G>A splice mutation at exon 5 donor splice site. *In silico* sequence analysis by the NNSplice and ASSP software tools predicts the activation of a weaker donor splice site (score 0.49 versus 1 of the canonical one) located 18 nucleotides downstream of the disrupted donor sequence. This might result in a partial intronic retention and elongation of exon 5 by six novel amino acids.

The diffuse NL observed in cells transfected with the p.Lys33Glu- and p.Arg42Trp-encoding cDNA indicated that these variants may impact the head domain of the protein and prevent proper formation of the lamina network. To address this hypothesis, we performed subcellular fractionation on transfected cells and the resulting nuclear and cytosolic fractions were analyzed by immunoblot (Figure 5). When analyzing the nuclear fraction only, a substantial reduction in the amount of lamin B1 recovered in the nuclear fraction of both the p.Lys33Glu- and p.Arg42Trp-transfected cell populations was observed (Figure 5A). The amount of nuclear lamin B1 recovered from the p.Ala152Gly-transfected cell population was also lower, possibly reflecting the overall decrease in steady-state levels of the variant form. The nuclear and cytosolic fractions were next analyzed in cells transfected with WT-, p.Lys33Glu-, p.Arg42Trp-, and p.Lys33Thr-encoding cDNA. The latter, p.Lys33Thr (c.98A>G), is a rare polymorphic variant (rs1303994586) that has been reported in gnomAD exomes with an allele frequency of 0.000008 (1/131,322 alleles), and so it served as a useful control for the specificity of the effects of the p.Lys33Glu variant. p.Lys33-Glu- and p.Arg42Trp-transfected cells, but not p.Lys33Thr-transfected cells, again showed a clear decrease in amount of lamin B1 within the nuclear fraction, along with a corresponding increase in lamin B1 within the cytosol fraction (Figure 5B), when compared to WT. Subsequent immunoblotting with lamin A/C and GAPDH antibodies

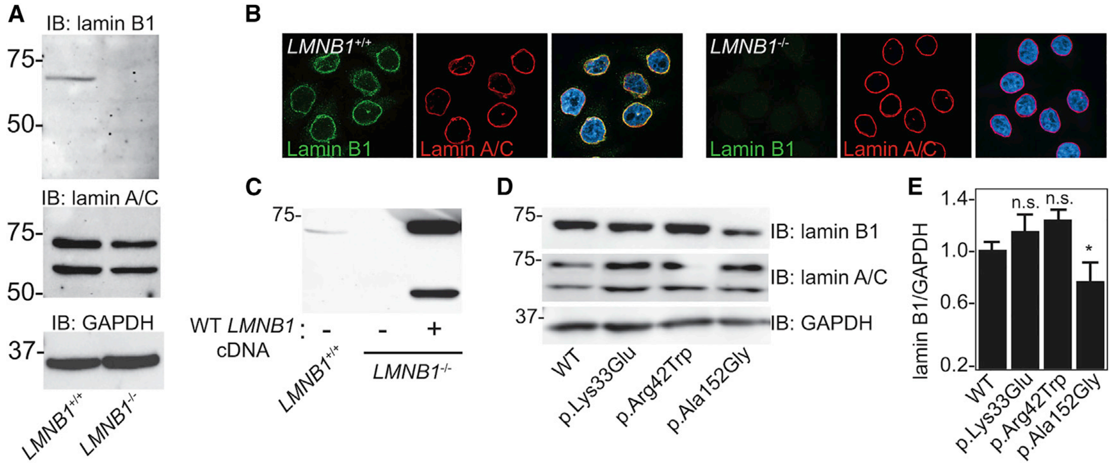

Figure 3. Validation of an *LMNB1*-Null HeLa Cell Line for Functional Characterization of *LMNB1* Variants

(A) Immunoblot analysis of lamin B1 and lamin A/C in parental (*LMNB1*$^{+/+}$) and *LMNB*1$^{-/-}$ HeLa cells. GAPDH was used to normalize protein loading.

(B) Immunostaining of lamin B1 (green) and lamin A/C (red) in HeLa cells. DAPI (blue) staining of the nucleus is shown in the merged images.

(C) Transfection of cDNA encoding WT *LMNB1* in the *LMNB*1$^{-/-}$ HeLa cells greatly increases the abundance of lamin B1 relative to *LMNB1*$^{+/+}$ HeLa cells.

(D) Expression of WT and variant-encoding cDNA in the *LMNB*1$^{-/-}$ HeLa cells followed by immunoblot analysis of whole-cell lysates.

(E) Quantification of the abundance of lamin B1 (relative to GAPDH) by densitometry in transfected HeLa cells (n = 4); *p ≤ 0.05.

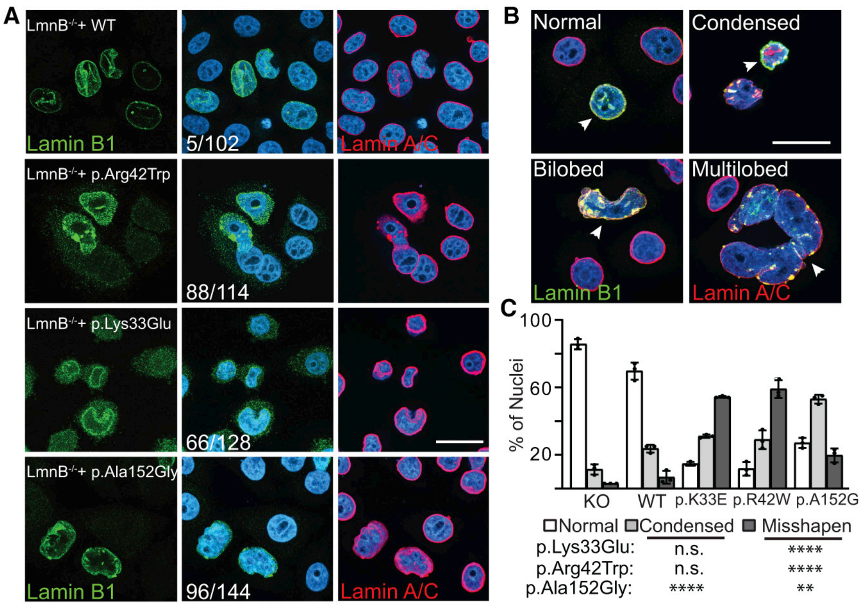

Figure 4. Introduction of Variant-Bearing *LMNB1* cDNAs Disrupts Nuclear Envelope Integrity

(A) Immunostaining of *LMNB1*$^{-/-}$ HeLa cells transfected with WT and variant-bearing *LMNB1* cDNAs (lamin B1, green; lamin A/C, red; DAPI, blue). The number of transfected cells with abnormal nuclear envelope morphology (versus the total cell quantified across at least four different fields from three independent staining experiments) is denoted in the middle panels. Scale bar represents 10 μm.

(B) Representative nuclear phenotypes observed in the transfected HeLa cells that were scored (the condensed phenotype was taken from the p.Ala152Gly cells and the bi-/multi-lobed phenotype was taken from the p.Lys33Glu cells); scale bar represents 10 μm.

(C) Quantification of the percentage of nuclei with a given phenotype from at least 100 cells scored across the three independent staining experiments; statistical analysis done with a Dunnett's test; $^{**}p \leq 0.01$, $^{****}p \leq 0.0001$.

demonstrated the fidelity of the subcellular fractionation. Quantification by densitometry of four independent experiments showed a 73 ± 10% and 65 ± 6% decrease in nuclear lamin B1 in the p.Lys33Glu- and p.Arg42Trp-transfected cells, respectively. A modest reduction in the amount of p.Lys33Thr lamin B1 from the nuclear fraction was noted, but there was no detectable lamin B1 in the cytosolic fraction (Figure 5D). Collectively, these findings indicate that p.Lys33Glu and p.Arg42Trp behave in a similar manner and result in improper formation of an NL when introduced alone in the *LMNB1*-null HeLa cells. Their increased abundance within the cytosolic fraction further suggests that the solubility of the lamin B1 monomers within this compartment increases when they fail to incorporate into the laminar network.

Next, we compared the impact of the LMNB1 p.Arg29Trp variant, recently reported in an individual with leukodystrophy and cerebellar involvement,

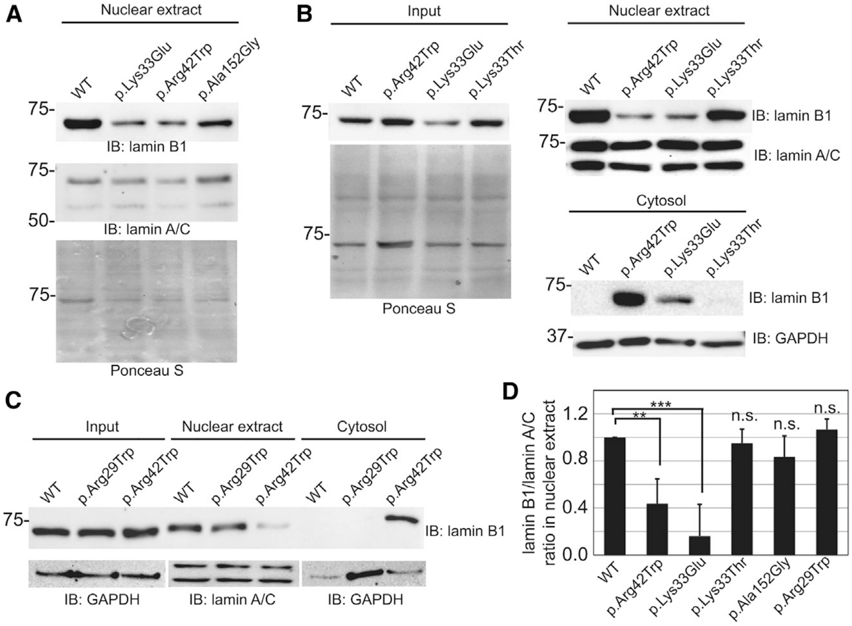

Figure 5. Increased Partitioning of p.Lys33Glu and p.Arg42Trp Lamin B1 into the Cytosol

(A) Immunoblot analysis of lamin B1 and lamin A/C in nuclear extracts from *LMNB1*$^{-/-}$ HeLa cells transfected with WT and variant-bearing *LMNB1* cDNAs ($n = 4$). Ponceau S staining is shown as a loading control.

(B) Immunoblot analysis of lamin B1 in whole-cell lysates of *LMNB1*$^{-/-}$ HeLa cells transfected with WT and variant-bearing *LMNB1* cDNAs. The same transfected cells were subjected to subcellular fractionation to isolate nuclei and cytosol. These fractions were resolved by SDS-PAGE and analyzed by immunoblot. Representative images from four independent experiments are shown.

(C) Immunoblot analysis of *LMNB1*$^{-/-}$ HeLa whole-cell lysates and nuclear and cytosolic fractions from these cells following transfection with WT-, p.Arg29Trp-, and p.Arg42Trp-encoding cDNAs. GAPDH and lamin A/C blots are shown below ($n = 3$).

(D) Collective quantification by densitometry of the ratio of lamin B1 to lamin A/C in nuclear extracts shown in (A)–(C). Values were normalized to the ratio observed with WT *LMNB1* cDNA (ratio was set at 1.0 for each condition). Error bars denote standard deviation of the mean; p values were determined via Student's t test ($^{**}p < 0.01$; $^{***}p < 0.001$).

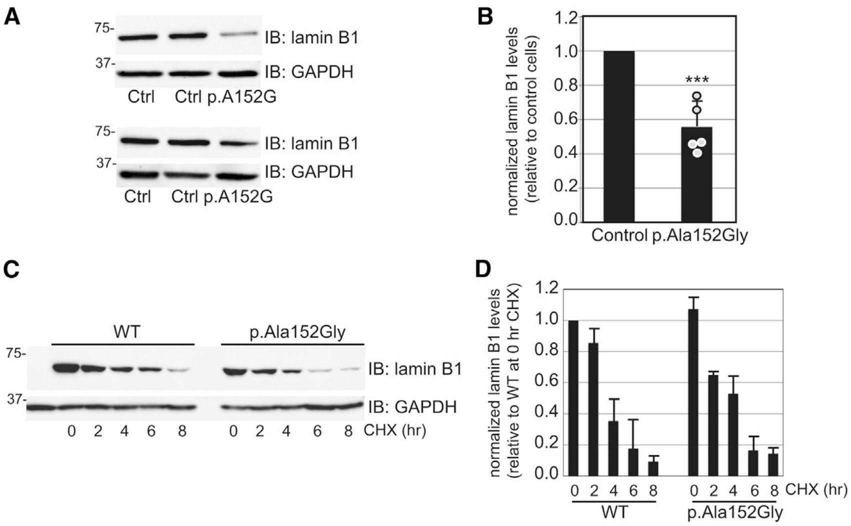

Figure 6. Reduced Steady-State Level of Lamin B1 in p.Ala152Gly Lymphoblasts

(A) Immunoblot analysis of lamin B1 in control and affected individual (p.Ala152Gly) lymphoblastoid cell lines. Representative results from two out of five independent experiments are shown.

(B) Quantification of the steady-state level of lamin B1 by densitometry and normalization to GAPDH levels ($n = 5$; statistical analysis performed via Student's t test; $^{***}p < 0.001$).

(C) *LMNB1*$^{-/-}$ HeLa cells transfected with WT- and p.Ala152Gly-encoding cDNAs were treated with cycloheximide for various times following lysis and analysis by SDS-PAGE and immunoblot. A representative blot from three independent experiments is shown.

(D) Quantification of lamin B relative to GAPDH (normalized to the WT 0 h cycloheximide treatment) from the three experiments is shown. Error bars represent standard deviations of the mean. No statistically significant differences in abundance were noted.

alongside the p.Arg42Trp variant by using the same experiment as above to evaluate whether these variants can be distinguished from each other with this assay. The results shown in Figure 5C (and quantified in Figure 5D) clearly demonstrate that only p.Arg42Trp leads to loss of integrity of the lamin B1 NL. This finding supports the notion that the p.Arg29Trp substitution is probably functionally distinct, resulting in a phenotype different from what is observed in the present cases.

Next, we sought to more clearly define the impact of the p.Ala152Gly variant and its mechanism of action and to confirm its effect on the steady-state level of lamin B1. Parallel sets of control and p.Ala152Gly proband-derived lymphoblasts were subjected to immunoblot analysis (Figure 6A) and the abundance of lamin B1 was quantified by densitometry (Figure 6B). As noted when the p.Ala152Gly variant encoding cDNA was introduced into the *LMNB1*-null HeLa cells, a decrease (56 ± 15% of control) in the steady-state level of lamin B1 was also observed in the proband lymphoblastoid cell lines (LCLs). This finding supports the instability of this variant lamin B1. In light of the fact that the individual has one normal *LMNB1* allele, it is possible that the variant form of the protein is degraded rapidly. We explored this mechanism in greater depth by treating *LMNB1*-null HeLa cells transfected with either WT- or p.Ala152Gly-encoding cDNA with cycloheximide to stop new protein translation and monitoring the loss of lamin B1 by immunoblot over time (Figure 6C). Although suggestive of enhanced turnover, quantification of three independent experiments failed to show a significant increase in the turnover of p.Ala152Gly compared to WT (Figure 6D).

Finally, the pronounced microcephaly and growth restriction seen in the individuals, together with the established role of lamin B1 in mitotic spindle formation, might point toward a spindle and/or mitotic defect underlying the microcephaly.[9,10,28] Using three proband-derived and two parental-control LCLs, we first analyzed the morphology of the nucleus in these cells, observing a significant increase in the number of cells with a bi-/multi-lobed phenotype in the p.Lys33Glu and p.Arg42Trp LCLs, confirming the observations in our HeLa system (Figure 7A). However, as shown in Figures 7B and 7C, the abnormal nuclear shape does not correlate with abnormal ploidy or failed mitotic segregation. In addition, we could not observe abnormal metaphase spindle formation in the proband LCLs compared to their parental controls.

In summary, we describe seven individuals presenting with severe microcephaly associated with cognitive deficit and neurological symptoms from five different families. Functional characterization of the three different missense variants demonstrated that these variants appear to disrupt the lamin B1 nuclear envelope when introduced into *LMNB1*-null HeLa cells, and there were variable effects on the lamin A/C NL. The two variants (p.Lys33Glu and p.Arg42Trp) that reside in the head region of the protein result in greatly increased recovery from the cytosol following subcellular fractionation, highlighting the importance of this domain in the formation of a stable, nuclear-localized laminar network. We speculate that mutation of lysine 33 is functionally relevant on a molecular level because this residue may be subject to acetylation as a regulatory mechanism. Although not a consensus site for any known post-translational modifications, the p.Arg42Trp variant might indirectly alter the modification of nearby phosphorylation or O-GlcNAc sites.

The p.Ala152Gly change did not result in increased cytosolic localization following subcellular fractionation, but this variant did disrupt nuclear envelope integrity when

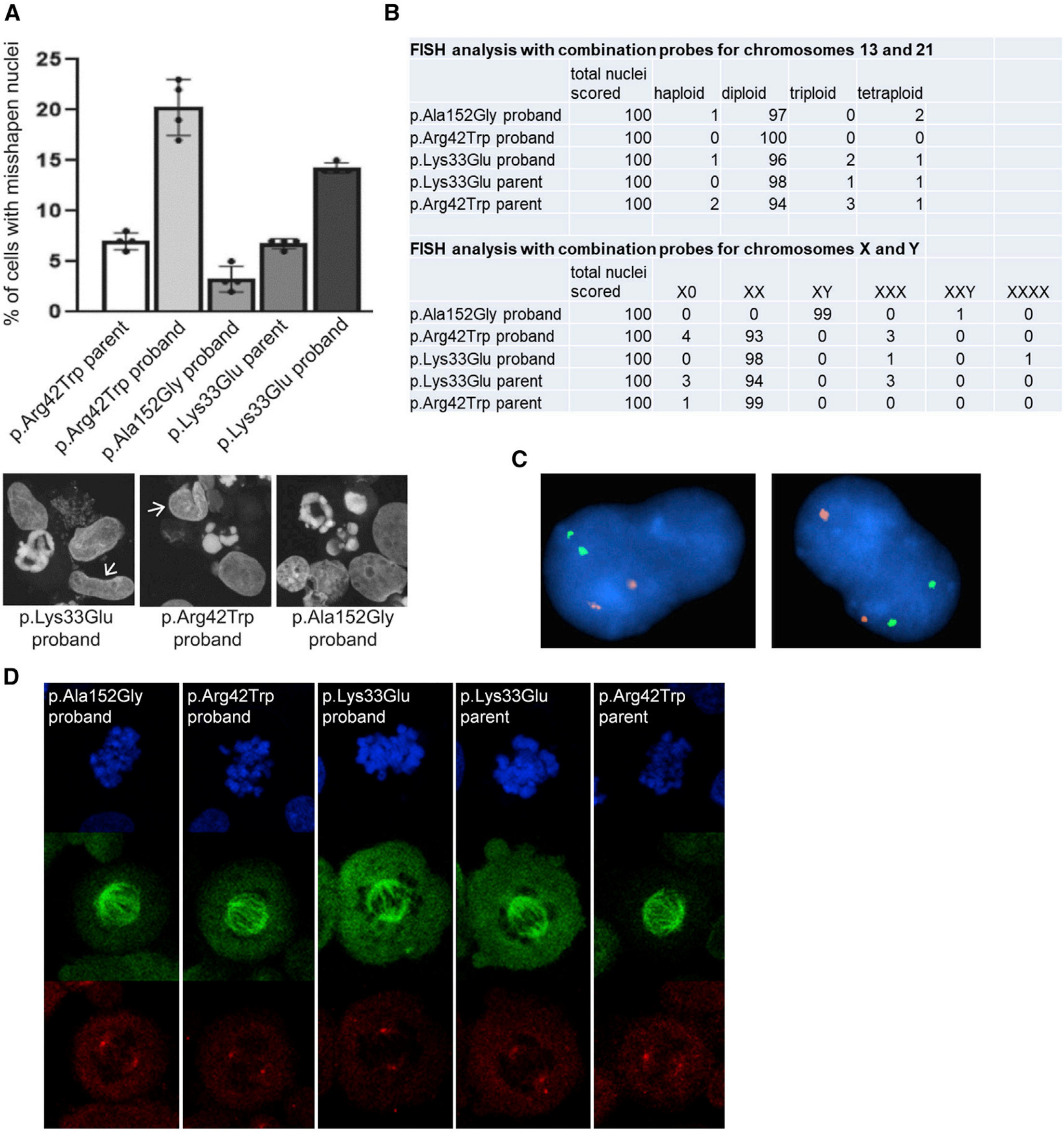

FISH analysis with combination probes for chromosomes 13 and 21

	total nuclei scored	haploid	diploid	triploid	tetraploid
p.Ala152Gly proband	100	1	97	0	2
p.Arg42Trp proband	100	0	100	0	0
p.Lys33Glu proband	100	1	96	2	1
p.Lys33Glu parent	100	0	98	1	1
p.Arg42Trp parent	100	2	94	3	1

FISH analysis with combination probes for chromosomes X and Y

	total nuclei scored	X0	XX	XY	XXX	XXY	XXXX
p.Ala152Gly proband	100	0	0	99	0	1	0
p.Arg42Trp proband	100	4	93	0	3	0	0
p.Lys33Glu proband	100	0	98	0	1	0	1
p.Lys33Glu parent	100	3	94	0	3	0	0
p.Arg42Trp parent	100	1	99	0	0	0	0

Figure 7. Abnormal Nuclear Shape in Proband-Derived Lymphoblast Cells Does Not Correlate with Abnormal Mitotic Spindle Formation or Ploidy Alteration

(A) Quantification of the percentage of nuclei with a misshapen phenotype from at least 100 proband-derived lymphoblast cells scored across three independent staining experiments and compared to control-parent-derived lymphoblast cells. Representative images of DAPI-stained nuclei from the different LCL populations are shown below the graph. Arrows indicate the misshapen nuclei. Note condensed nuclei in the p.Ala152Gly LCL.

(B) Overview of ploidy screening results in 100 nuclei per LCL via two different fluorescence *in situ* hybridization (FISH) probe mixtures showing no difference between proband and parental control lines.

(C) Representative image of interphase FISH analysis with chromosomes 13/21 probe mixture showing normal diploid bi-lobed nuclei.

(D) Representative images of normal metaphase spindles stained with antibodies against α-tubulin (green) and γ-tubulin (red). At least 20 spindles were scored per LCL and no difference in morphology could be noted between proband and parental control cells.

introduced into the *LMNB1*-null HeLa cells. Localized to one of the coil domains, it is possible that this variant alters the conformation of lamin B1 in a way that weakens the NL. In addition, unlike the other variants, p.Ala152Gly seemed to have a more pronounced effect on the integrity of the lamin A/C envelope, which may indicate it alters nuclear envelope structure more globally. In the two other families, which include individuals 2 and 5–7 with the intragenic p.Ser314_Thr497 deletion and the splice mutation c.939+1G>A, respectively, we hypothesize an equally dominant-negative effect of the resulting abnormal lamin B1. The p.Ser314_Thr497 deletion affects the NLS, and one could again foresee insufficient protein abundance in the nucleus to form a stable laminar network.

In human neurons, where lamin B1 is more abundant, impaired nuclear envelope integrity can result in a spectrum of negative consequences that ultimately lead to microcephaly in affected individuals. As already shown by the work of the Young SG lab, cortical neurons in lamin-B1-deficient mice show abnormal migration resulting in abnormal cortical layering, a phenotype similar to the simplified gyration seen on MRI in our affected individuals.[13,14] In addition, the same group more recently showed that absence of lamin B1 results in a weakened nuclear envelope, impairing nucleokinesis and leading to reduced neuronal survival.[11] Disruption of nuclear envelope integrity, as observed for the different variants, might not only interfere with the disassembly and assembly on the lamina during cell division, but also impact the survival and migration of neural precursors and hence lead to severe reduction of brain size. In addition, the role of lamin B1 in mitotic spindle formation might also point toward a spindle and/or mitotic defect underlying the microcephaly. Although we could not confirm this in the different proband lymphoblastoid cells, we cannot exclude this pathomechanism in other cell types, including neurons. Finally, alterations in the expression of genes that drive neurogenesis can arise in neuronal cells when contacts between the NL and chromatin are lost.[10]

In light of the multiple domains within the *LMNB1* gene product, it is feasible that different missense variants will impact lamin B1 function by unique mechanisms, and thus, case-by-case functional analysis is warranted. The present work also adds *LMNB1* to the growing list of genes implicated in severe autosomal-dominant microcephaly.

Data and Code Availability

All variants described in the study have been deposited in ClinVar: accession numbers SCV001296959–SCV001296963.

Supplemental Data

Supplemental Data can be found online at https://doi.org/10.1016/j.ajhg.2020.08.015.

Acknowledgments

The authors thank the patients and their families for their cooperation. We are also grateful to K. Van den Bogaert and W. Huybrechts for technical assistance. We acknowledge the contributions of Henrietta Lacks and her family to the research. F.C. received a PhD fellowship from and H.V.E. is a clinical investigator of the Fund for Scientific Research Flanders (FWO-Vlaanderen), Belgium. R.S. and H.F.-S. are supported by a grant from the National Institutes of Health (5R01GM086524-11) and the Greenwood Genetic Center. J.R.V. is supported by FWO-Vlaanderen (GOE1117N) and KU Leuven (C14/18/092). The authors thank the Telethon Undiagnosed Diseases Program (GSP15001) and its members. The authors declare that there are no conflicts of interest.

Declaration of Interests

The authors declare no competing interests.

Received: March 27, 2020
Accepted: August 18, 2020
Published: September 9, 2020

Web Resources

Alternative Splice Site Predictor (ASSP), http://wangcomputing.com/assp/
ClinVar, https://www.ncbi.nlm.nih.gov/clinvar/
dbSNP, https://www.ncbi.nlm.nih.gov/snp/
Decipher, https://decipher.sanger.ac.uk/
Ensembl, http://www.ensembl.org/index.html
Genic intolerance, http://genic-intolerance.org/index.jsp
gnomAd, https://gnomad.broadinstitute.org/
HLBI Exome Sequencing Project (ESP) Exome Variant Server, https://evs.gs.washington.edu/EVS/
Human Splicing Finder 3.1, https://www.genomnis.com/access-hsf
Leiden Open Variation Database v.3.0, https://www.lovd.nl/
MutationTaster, http://mutationtaster.org/
NNSplice v.0.9, https://www.fruitfly.org/seq_tools/splice.html
OMIM, https://www.omim.org/
PolyPhen2, http://genetics.bwh.harvard.edu/pph2/
Provean (protein variation effect analyzer), http://provean.jcvi.org/index.php

References

1. Worman, H.J. (2012). Nuclear lamins and laminopathies. J. Pathol. *226*, 316–325.
2. Dechat, T., Pfleghaar, K., Sengupta, K., Shimi, T., Shumaker, D.K., Solimando, L., and Goldman, R.D. (2008). Nuclear lamins: major factors in the structural organization and function of the nucleus and chromatin. Genes Dev. *22*, 832–853.
3. Burke, B., and Stewart, C.L. (2013). The nuclear lamins: flexibility in function. Nat. Rev. Mol. Cell Biol. *14*, 13–24.
4. Davidson, P.M., and Lammerding, J. (2014). Broken nuclei–lamins, nuclear mechanics, and disease. Trends Cell Biol. *24*, 247–256.
5. Pascual-Reguant, L., Blanco, E., Galan, S., Le Dily, F., Cuartero, Y., Serra-Bardenys, G., Di Carlo, V., Iturbide, A., Cebrià-Costa, J.P., Nonell, L., et al. (2018). Lamin B1 mapping reveals the existence of dynamic and functional euchromatin lamin B1 domains. Nat. Commun. *9*, 3420.
6. Hah, J., and Kim, D.-H. (2019). Deciphering Nuclear Mechanobiology in Laminopathy. Cells *8*, 231.
7. Stewart, C., and Burke, B. (1987). Teratocarcinoma stem cells and early mouse embryos contain only a single major lamin polypeptide closely resembling lamin B. Cell *51*, 383–392.
8. Röber, R.A., Weber, K., and Osborn, M. (1989). Differential timing of nuclear lamin A/C expression in the various organs of the mouse embryo and the young animal: a developmental study. Development *105*, 365–378.
9. Vergnes, L., Péterfy, M., Bergo, M.O., Young, S.G., and Reue, K. (2004). Lamin B1 is required for mouse development and nuclear integrity. Proc. Natl. Acad. Sci. USA *101*, 10428–10433.
10. Kim, Y., Sharov, A.A., McDole, K., Cheng, M., Hao, H., Fan, C.-M., Gaiano, N., Ko, M.S.H., and Zheng, Y. (2011). Mouse B-type lamins are required for proper organogenesis but not by embryonic stem cells. Science *334*, 1706–1710.
11. Chen, N.Y., Yang, Y., Weston, T.A., Belling, J.N., Heizer, P., Tu, Y., Kim, P., Edillo, L., Jonas, S.J., Weiss, P.S., et al. (2019). An

absence of lamin B1 in migrating neurons causes nuclear membrane ruptures and cell death. Proc. Natl. Acad. Sci. USA *116*, 25870–25879.

12. Coffinier, C., Fong, L.G., and Young, S.G. (2010). LINCing lamin B2 to neuronal migration: growing evidence for cell-specific roles of B-type lamins. Nucleus *1*, 407–411.
13. Coffinier, C., Jung, H.J., Nobumori, C., Chang, S., Tu, Y., Barnes, R.H., 2nd, Yoshinaga, Y., de Jong, P.J., Vergnes, L., Reue, K., et al. (2011). Deficiencies in lamin B1 and lamin B2 cause neurodevelopmental defects and distinct nuclear shape abnormalities in neurons. Mol. Biol. Cell *22*, 4683–4693.
14. Young, S.G., Jung, H.J., Coffinier, C., and Fong, L.G. (2012). Understanding the roles of nuclear A- and B-type lamins in brain development. J. Biol. Chem. *287*, 16103–16110.
15. Young, S.G., Jung, H.-J., Lee, J.M., and Fong, L.G. (2014). Nuclear lamins and neurobiology. Mol. Cell. Biol. *34*, 2776–2785.
16. Lee, J.M., Tu, Y., Tatar, A., Wu, D., Nobumori, C., Jung, H.J., Yoshinaga, Y., Coffinier, C., de Jong, P.J., Fong, L.G., and Young, S.G. (2014). Reciprocal knock-in mice to investigate the functional redundancy of lamin B1 and lamin B2. Mol. Biol. Cell *25*, 1666–1675.
17. Lee, J.M., Jung, H.J., Fong, L.G., and Young, S.G. (2014). Do lamin B1 and lamin B2 have redundant functions? Nucleus *5*, 287–292.
18. Giacomini, C., Mahajani, S., Ruffilli, R., Marotta, R., and Gasparini, L. (2016). Lamin B1 protein is required for dendrite development in primary mouse cortical neurons. Mol. Biol. Cell *27*, 35–47.
19. Mahajani, S., Giacomini, C., Marinaro, F., De Pietri Tonelli, D., Contestabile, A., and Gasparini, L. (2017). Lamin B1 levels modulate differentiation into neurons during embryonic corticogenesis. Sci. Rep. *7*, 4897.
20. Gigante, C.M., Dibattista, M., Dong, F.N., Zheng, X., Yue, S., Young, S.G., Reisert, J., Zheng, Y., and Zhao, H. (2017). Lamin B1 is required for mature neuron-specific gene expression during olfactory sensory neuron differentiation. Nat. Commun. *8*, 15098.
21. Yang, S.H., Jung, H.J., Coffinier, C., Fong, L.G., and Young, S.G. (2011). Are B-type lamins essential in all mammalian cells? Nucleus *2*, 562–569.
22. Padiath, Q.S., Saigoh, K., Schiffmann, R., Asahara, H., Yamada, T., Koeppen, A., Hogan, K., Ptácek, L.J., and Fu, Y.-H. (2006). Lamin B1 duplications cause autosomal dominant leukodystrophy. Nat. Genet. *38*, 1114–1123.
23. Pedroso, J.L., Munford, V., Bastos, A.U., Castro, L.P., Marussi, V.H.R., Silva, G.S., Arita, J.H., Menck, C.F.M., and Barsottini, O.G. (2017). LMNB1 mutation causes cerebellar involvement and a genome instability defect. J. Neurol. Sci. *379*, 249–252.
24. Sobreira, N., Schiettecatte, F., Valle, D., and Hamosh, A. (2015). GeneMatcher: a matching tool for connecting investigators with an interest in the same gene. Hum. Mutat. *36*, 928–930.
25. Anna, A., and Monika, G. (2018). Splicing mutations in human genetic disorders: examples, detection, and confirmation. J. Appl. Genet. *59*, 253–268.
26. Reese, M.G., Eeckman, F.H., Kulp, D., and Haussler, D. (1997). Improved splice site detection in Genie. J. Comput. Biol. *4*, 311–323.
27. Wang, M., and Marín, A. (2006). Characterization and prediction of alternative splice sites. Gene *366*, 219–227.
28. Tsai, M.Y., Wang, S., Heidinger, J.M., Shumaker, D.K., Adam, S.A., Goldman, R.D., and Zheng, Y. (2006). A mitotic lamin B matrix induced by RanGTP required for spindle assembly. Science *311*, 1887–1893.

The American Journal of Human Genetics, Volume *107*

Supplemental Data

De Novo Variants in *LMNB1* Cause Pronounced Syndromic Microcephaly and Disruption of Nuclear Envelope Integrity

Francesca Cristofoli, Tonya Moss, Hannah W. Moore, Koen Devriendt, Heather Flanagan-Steet, Melanie May, Julie Jones, Filip Roelens, Carmen Fons, Anna Fernandez, Loreto Martorell, Angelo Selicorni, Silvia Maitz, Giuseppina Vitiello, Gerd Van der Hoeven, Steven A. Skinner, Mathieu Bollen, Joris R. Vermeesch, Richard Steet, and Hilde Van Esch

Supplemental Note: Case Reports

Case 1

Individual 1 is the second child of healthy, unrelated Belgian parents. Pregnancy was uneventful, but prenatal ultrasound showed small head circumference. Birth parameters at term included a weight of 2610 g, length 46 cm and very small head circumference of 25 cm (-4.6 SD).

Brain MRI at ages 6 and 18 months showed besides the extreme microcephaly a small corpus callosum. Development of the child was delayed with independent walking at age 2.5 years and diagnosis of moderate intellectual delay and autism at the age of 4 years.

At the last clinical evaluation, age 9.5 years, his weight was 16 kg (-1.94 SD), length 122 cm (-2.7 SD), and head circumference 42 cm (-6.8 SD). He is still making slow progress, e.g. using few words and short sentences, being able to read individual characters and a few words, riding a tricycle. Clinical examination showed besides the microcephaly a mild hypertonia in hamstrings and triceps surae and mild hyperreflexia.

Case 2

Individual 2 is the first child of unrelated Belgian parents. She has an older paternal and maternal brother, both healthy. Pregnancy was uneventful, but prenatal ultrasound showed small head circumference. Birth parameters at term included a weight of 3460 g, length 51 cm and head circumference of 32 cm (-1.9 SD). She had a delayed development with independent walking at age 2 years and slow language acquisition. Re-examination at age 9 years and 4 months showed a mild to moderately delayed girl with microcephaly (-3.7 SD), and mild dysmorphic features. She follows special education. The microdeletion involving part of the *LMNB1* gene is inherited from her mother. The adult head circumference of the mother is 50.3 cm (- 2.7 SD). The mother followed normal school with extra support.

Case 3

Individual 3 is the fourth child of healthy, non-consanguineous Italian parents. The three sisters are healthy. Prenatal ultrasound showed microcephaly and amniocentesis was performed showing a normal fetal karyotype (46,XX). Delivery was via caesarean section at 35 weeks of gestation because of previous sections and maternal pain. At birth, length and weight were 2190 g (24th centile) and 42 cm (4th centile), respectively, while head circumference was 28 cm (<3rd centile, -2.8 SD). Growth remained severely delayed for all parameters, with absolute microcephaly. Re-examination at age 5 years and 7 months showed a severely delayed girl with severe microcephaly. She has not achieved the sitting position, neither any language. Brain MRI at this age shows pachygyria and lissencephaly. Postnatal standard karyotype, and molecular karyotyping were both normal.

Case 4

Individual 4 was last evaluated at the age of 2 years and 8 months. Pregnancy history was significant for preterm labour at 28 weeks gestation, at which time microcephaly was noted. The mother was placed on bedrest and delivery was at 38-5/7 weeks. Head circumference at birth measured 29 cm (-4 SD). Work-up during and after the pregnancy for TORCH infections and Zika virus were negative. Seizure activity began within the first day of life. A brain MRI performed on day 2 of life showed a simplified gyral pattern and dysgenesis of the corpus callosum. Seizures have been relatively well controlled with anti-epileptic medications. Because of recurrent pneumonia, presumably due to aspiration, a G-tube was placed. Other medical history includes cortical visual impairment and chronic constipation. She presented with a significant developmental delay. At 2 years 8 months, she had good head control and was able to sit in a tripod position with support, swing her arms but not yet reach or grab, and she was making noises. Severe microcephaly continues to be noted while length is tracking slightly below the 1st percentile and weight is at the 14th percentile. Family history is unremarkable.

Cases 5, 6, 7

Individuals 5, 6 and 7 belong to the same Arabic sibship. Individual 5 is the youngest of healthy, unrelated parents. Pregnancy was uneventful. At 20 months of age, her weight was 6.210 kg (-4.5 SD), height: 77 cm (-2.4 SD), and head circumference 45 cm (-4.42 SD). At clinical examination, microcephaly, severe development delay with axial hypotonia, mild scoliosis, and lack of language and communication interest was noted. She has two older and equally affected brothers. Individual 6 is the firstborn of the couple. Prenatal ultrasound at PMA of 30 weeks showed a small head circumference. Delivery occurred via C-section because of foetal bradycardia. Weight at birth was 2.500 gr (-2.3 SD), no other anthropometric birth parameters are available. He presented with severe microcephaly and seizure onset at 14 days of life. He gradually developed a spastic tetraparesis in association with severe axial hypotonia without control of the head. At clinical evaluation (when he was admitted to the genetic centre in Barcelona for a second opinion, age 11 years), his weight was 28 kg (-1.37 SD), height: 122 cm (-4,07 SD), BMI: 18.79 kg/m2 (-0.07 SD), and head circumference 40 cm (-10 SD). Besides the severe microcephaly, he showed long eyelashes, a high palate, gingival thickening and hypertrichosis. He has no language and motor dysfunction GMFCS level V. Currently, he has no longer epileptic seizures and antiepileptic treatment was stopped. Because of an aspiration pneumonia secondary to dysphagia and gastroesophageal reflux a G-tube was placed.

Brain MRI (11 years) showed a simplified gyral pattern, prominent extra-axial spaces, dilated ventricles related to the low volume of the brain. Cerebellum and brainstem were preserved. A metabolic work-up was negative. Molecular karyotype showed the presence of 280 kb duplication on chromosome 17p13.3, which is considered as a variant of unknown significance, not present in the other affected brother. A gene panel specific for infantile epileptic encephalopathy did not demonstrate pathogenic mutations.

The younger brother, individual 7, and the second child of this couple, showed a highly similar clinical course. At clinical evaluation (age 10 years), his weight was 29 kg (-0.79 SD), height: 125.34 cm (-2,50 SD), BMI 18.46 kg / m2 (0,15 SD), and head circumference 39 cm (-10 SD). He also has a severe developmental delay with spastic tetraparesis, scoliosis and no language. Brain imaging showed the same simplified gyral pattern, as seen in his older brother. He still has seizures that are well controlled with valproate, levetirazetam, and clobazam. Additional metabolic examinations and molecular karyotype were normal in this individual.

Supplemental Table 1

Summary of sequencing platforms and coverage in four unrelated families reported with a *LMNB1* variant

	Individual 1	**Individual 3**	**Individual 4**	**Individuals 5-7**
Sequencing laboratory	Center for Human Genetics, UZ Leuven, Belgium	TIGEM Institute, Pozzuoli, Naples, Italy	Greenwood Genetic Center, USA	Bio Array Alicante, Spain
Sequencing type	Trio exome sequencing + Sanger sequencing of *LMNB1* in proband and parents	Trio exome sequencing + Sanger sequencing of *LMNB1* in proband and parents	Trio exome sequencing + Sanger sequencing of *LMNB1* in proband and parents	Trio exome sequencing + Sanger sequencing of *LMNB1* in probands and parents
Capture and library construction	Roche SeqCap EZ Exome Enrichment v.3.0	Agilent SureSelect Clinical Research Exome v2	Agilent SureSelectXT Clinical Research Exome v2	Agilent SureSelect Clinical Research Exome v2
Sequencing platform	Illumina HiSeq2500	Illumina NextSeq500	Illumina NextSeq500	Illumina NovaSeq
Average depth of targeted bases	80X	125X	259X	125X
Percentage of bases covered >10x	94.0%	96.40%	97.0%	96.4%
Target of analysis	Whole exome	Whole exome	Whole exome	Custom gene panels: microcephaly (~800 genes), epilepsy (~1200 genes) and cerebral atrophy (~250 genes)

Overview of *de novo* variants identified by WES in individuals 1, 3-4

ID	**Gene**	**Chr**	**Genomic position**	**REF allele**	**ALT allele**	**HGVS**	**dbSNP**
Individual 1	*LMNB1*	5	126140563	C	G	NM_005573.3:ex2:c.455C>G:NP_005564.1:p.Ala152Gly	-
Individual 1	*RAD51C*	17	56774110	A	G	NM_058216.3:ex3:c.461A>G:NP_478123.1:p.Glu154Gly	rs758847241
Individual 3	*LMNB1*	5	126113297	A	G	NM_005573.3:ex1:c.97A>G:NP_005564.1:p.Lys33Glu	-
Individual 3	*TMEM218*	11	124967600	G	C	NM_001080546.2:ex5:c.250C>G:NP_001074015.1:p.Leu84Val	-
Individual 3	*CACNA1I*	22	40030701	C	T	NM_001003406.1:ex5:c.712C>T:NP_001003406.1:p.Arg238Cys	-
Individual 4	*LMNB1*	5	126113324	C	T	NM_005573.3:ex1:c.124C>T:NP_005564.1:p.Arg42Trp	-
Individual 4	*SEPT14*	7	55910834	T	G	NM_207366.2:ex5:c.372-13A>C	-
Individual 4	*RBM19*	12	114392971	C	T	NM_001146699.1:ex7:c.886G>A:NP_001140171.1:p.Val296Met	rs1409746316

Chr: chromosome; REF allele: reference allele; ALT allele: alternative allele;

Supplemental Table 2

Pathogenicity scores of missense and splice variant

Software	Variant & Score	Classification comment
PolyPhen2 (HumVar score)	p.Ala152Gly: 0.77 p.Lys33Glu: 1 p.Arg42Trp: 1 c.939+1G>A	Possibly damaging Probably damaging Probably damaging NA
PROVEAN	p.Ala152Gly: -3.67 p.Lys33Glu: -3.29 p.Arg42Trp: -6.67 c.939+1G>A	Deleterious Deleterious Deleterious NA
MutationTaster	p.Ala152Gly: 60 p.Lys33Glu: 56 p.Arg42Trp: 101 c.939+1G>A: NA	Disease causing Disease causing Disease causing Disease causing
GERP++	p.Ala152Gly: 5.15 p.Lys33Glu: 2.72 p.Arg42Trp: 2.72 c.939+1G>A: 5.84	Highly constrained Constrained Constrained Highly constrained
PhastCons100 (vertebrate)	p.Ala152Gly: 1 p.Lys33Glu: 1 p.Arg42Trp: 1 c.939+1G>A: 1	Conserved Conserved Conserved Conserved
dbscSNV **ADA score** **RF score**	c.939+1G>A: 0.99 c.939+1G>A: 0.938	Splice-altering Splice-altering
HSF 3.1	c.939+1G>A	Broken WT donor site

Pathogenicity predictions. A summary of the pathogenicity predictions and conservation scores for each missense and splice-site mutation generated using the following pathogenicity prediction software tools:

PolyPhen2 (http://genetics.bwh.harvard.edu/pph2/)

PROVEAN (http://provean.jcvi.org/index.php)

MutationTaster (http://mutationtaster.org/)

GERP++ and PhastCons100 conservation scores have been retrieved from the corresponding tracks in the UCSC Genome Browser (https://genome.ucsc.edu/).

Splice-site predictions for the c.939+1G>A mutation have been generated using Human Splicing Finder (HSF) 3.1 software tool (http://www.umd.be/HSF/) or retrieved from the Ensembl Variant Effect Predictor tool (http://grch37.ensembl.org/Homo_sapiens/Tools/VEP).

Supplemental Materials and Methods

Cell culture: WT and *LMNB1*$^{-/-}$ Hela cells (Canopy Biosciences, Saint Louis, MO) were cultured in DMEM (ThermoFisher; #10-017-CV) supplemented with 10% fetal bovine serum (VWR; #97068-085) and 1% penicillin/streptomycin (ThermoFisher; #30-002-CI) in a 5% CO_2 humidified tissue culture incubator. The *LMNB1*$^{-/-}$ Hela cells, generated using CRISPR-Cas9 editing, contain a 2bp deletion in exon 1 on the first allele and a 2bp insertion in exon 1 on the second allele.

We derived lymphoblast cell lines of the probands with the p.Lys33Glu, p.Ala152Gly and p.Arg42Trp mutations, as well as from one healthy parent of proband p.Lys33Glu and a healthy parent of proband p.Arg45Trp. These parental lines served as controls. Control and proband lymphoblast cells were cultured in RPMI 1640 (ThermoFisher; #10-040-CV) supplemented with 10% fetal bovine serum (VWR; #97068-085), 1% antibiotic/antimycotic (Sigma A5955), L-Glutamine (Sigma G7513) in a 5% CO_2 humidified tissue culture incubator.

Transfection: Expression constructs for the different *LMNB1* variants were generated by site-directed mutagenesis. The cDNA sequence change for each variant is: p.Lys33Glu (c.97A>G), p.Lys33Thr (c.98A>G), p.Arg42Trp (c.124C>T), p.Ala152Gly (c.455C>G), and p.Arg29Trp (c.85C>T). 500,000 cells were plated per well in a 6 well dish 18h prior to transfection in growth media. The cells were rinsed with PBS followed by addition of 0.5 mL of OptiMEM (ThermoFisher; #31985062) and then transfected with 5µg of plasmid and 10µl Lipofectamine 2000 (ThermoFisher; #11668019) per well OptiMEM. After 5h, the media was replaced with 1 ml of OptiMEM and the cells collected 24 h post-transfection for analysis. For more facile comparison, we choose to use the protein variant (instead of the nucleotide change) when describing the HeLa transfection results in the main text.

Subcellular Fractionation: Cells were fractionated into nuclear and cytosolic fractions using the following protocol. Aliquots of the same cells were reserved in order to determine transfected protein input. All steps were performed on ice and centrifugation at 4°C. Subcellular fractionation buffer (SF buffer) containing 250 mM sucrose, 10 mM KCl, 20 mM HEPES (pH 7.4), 1.5 mM $MgCl_2$, and 1 mM EDTA, 1mM DTT, and protease inhibitor cocktail, was added to trypsinized cell pellets to generate homogenates. Homogenates were passed through a 25-gauge needle ten times before centrifugation at 8,000 rpm (10,000 x g) for 12 min resulting in a pellet containing nuclei, and a cytosolic supernatant fraction. RIPA buffer was added to the fractionated cellular components to solubilize the proteins and a BCA assay was performed to quantify total protein concentration in each fraction.

SDS-PAGE and Western Blot Analysis: Cells were released from the culture plates using trypsin and lysed in cold lysis buffer (50mM Tris-HCl pH 8.0, 150mM NaCl, 1% NP-40, 0.1% SDS, 0.5% sodium deoxycholate), with protease inhibitors (ThermoFisher; #A32955) and 2mM DTT. Following incubation for 30 min on ice, and vortexing for 20 sec, the cells were centrifuged at 20,000xg for 10 min at 4°C. Total protein was quantified in the supernatant using the Micro BCA Protein Assay (ThermoFisher; #23235). 60 µg of cell lysate per sample and 5 µl of 10x concentrated media was prepared in Lamelli buffer, incubated at 95°C for 5 min and chilled at 4°C. Samples were separated on an 8% SDS-PAGE gel. Protein was transferred to 0.45uM pore nitrocellulose (Abersham; #10600004) at 110 volts for 2h at 4°C in transfer buffer. The membrane was rinsed and stained with Ponceau S for normalization. The membranes were blocked with 5% milk/TBST for 1h at room temperature. LMNB1 western blots were incubated with HRP conjugated anti-rabbit antibody (Jackson ImmunoResearch; #111-035-144) at 1:1000 overnight at 4°C, washed 3x with TBST, and developed with SuperSignal West Pico PLUS ECL reagent (ThermoFisher; #34577). All images were captured on the Bio-Rad ChemiDoc MP

Imaging System (Bio-Rad; #12003154). Analysis was done with Image Lab Software (Bio-Rad #1709690, ver5.2.1).

Immunostaining and confocal microscopy: HeLa cells were seeded onto coverslips in a twelve well cell culture plate. After washing with Dulbecco's PBS (DPBS) containing calcium and magnesium, the cells were fixed to the slides with the addition of 3.7% formaldehyde for 10 mins followed by washing 4 times in DPBS containing calcium and magnesium. Permeabilization was achieved with the addition of 1 mL of 0.1% Triton-X in DPBS for 10 mins at room temperature and then wells were washed three times with DPBS containing calcium and magnesium. Fixed coverslips were blocked using 3% bovine serum albumin and incubation for 1 h at room temperature on a rotator followed by washing with DPBS. A rabbit monoclonal anti-lamin B1 antibody from Cell Signaling Technology (D9V6H; cat # 13435; 1:1000 dilution in WT and KO HeLa and 1:4000 in transfected KO cells) and mouse monoclonal anti-lamin A/C antibody from Santa Cruz Biotechnology (cat #: SC-7292; 1:1000 dilution) were added for 1 h at room temperature followed by incubation with an Alexa Fluor 488 goat anti-rabbit IgG or Alexa Fluor 568 anti-mouse IgG secondary antibody (Abcam, 1:500 dilution) in the dark for 1 hr. After washing, the coverslips were mounted with Prolong Gold^{TM} containing DAPI and visualized using an Olympus FV3000 confocal microscope. For quantification of the different nuclear and nuclear envelope phenotypes, at least one hundred cells were counted on slides from three independent experiments and the percentage of cells with each phenotype averaged. Statistical analysis was performed using a Dunnett's t test.

Polyploidy screening via Fluorescence in situ hybridization: Fixed cells were pre-treated for 10 min with 0.1 mg pepsin/ml (Sigma) in 0.01 mol/l HCl at 37°C followed by a 3 min wash in 1 x PBS. Post-fixation was performed by incubating the slides for 10 min in a 1% formaldehyde solution with 0.05 mol/l MgCl2 and 1 x PBS at 4°C. Slides subsequently were washed in 1 x

PBS and dehydrated by ethanol series. Then 5µl of probe mixture was applied to the slide, covered with a coverslip (10mm x 10mm) and sealed with rubber cement. We used the probe mixtures: Séq uniques 13/21 (Cytocell, 13q14.2/21q22.13, Spectrum Green/Spectrum Orange), and CEPXY (Vysis, Xp11.1-q11.1 Alpha Satellite DNA/Yq12 Satellite III, Spectrum Green/Spectrum Orange). Nuclei and probe were denatured simultaneously on a hot plate at 75°C for 5 min. Hybridization was allowed to take place overnight in a humid chamber at 37°C. After hybridization, excess or non-specific bound probe was removed by subsequent washes in 0.4 x SSC/0.3% NP-40 (73°C for 1 min), 2 x SSC/0.1% NP-40 (room temperature for 1 min) and 2 x SSC (room temperature for 1 min) followed by dehydration through ethanol series. After drying, the slides were mounted in Vectashield anti-fading medium (Vector Laboratories, Peterborough, UK) containing 2.5 ng/ml 40,6-diamidino-2-phenylindole (DAPI; Boehringer Ingelheim GmbH, Germany). Nuclei were examined using an Axioplan 2 microscope (Zeiss NV, Zaventem).

Metaphase mitotic spindle analysis: Control and proband lymphoblast cells were cultured in RPMI 1640 (ThermoFisher; #10-040-CV) supplemented with 10% fetal bovine serum (VWR; #97068-085), 1% antibiotic/antimycotic (Sigma A5955), L-Glutamine (Sigma G7513) in a 5% CO_2 humidified tissue culture incubator. Next we used the protocol as described by Qian et al., 2017 [1]. For RO3306 washout experiments, cells were initially treated with 2mM thymidine for 24 h, washed with PBS, and released in fresh medium for 4 h prior to treatment with 9 µM RO3306. After 12 h, the cells were washed with PBS and incubated with fresh medium containing 10µM MG132 for 90 min.

Cells were transferred to a glass slide using the Tharmac CellSpin I (5’ 500rpm) and fixed with 4% paraformaldehyde, permeabilized with 0.5% Triton X-100 and blocked in 3% BSA/PBS. Cells were subsequently incubated with primary antibodies [alpha-Tubulin diluted at 1/1000 - Sigma-Aldrich, cat n° T6074 and gamma-Tubulin diluted at 1/500 – Abcam, cat n° ab11317] in

1.0% BSA/PBS for 2 h at room temperature and with secondary antibodies for 1 h at room temperature. DNA was stained with DAPI. Confocal images were acquired with a Leica TCS SPE laser-scanning confocal system mounted on a Leica DMI 4000B microscope, and equipped with a Leica ACS APO 63X 1.30NA oil DIC objective. For quantification, Z stack scans were performed through each cell (4-6 sections, 1 µm intervals), and analyzed using ImageJ software and the Z project ‘sum slices’ feature.

Supplemental Reference

1. Qian, J.,García-Gimeno, M.A., Beullens, M., Manzione, M., G., Igual, J.C., Heredia, M., Sanz, P., Gelens, L., Bollen, M. (2017). An Attachment-Independent Biochemical Timer of the Spindle Assembly Checkpoint. Mol. Cell *68*, 715-73.